A velocity map imaging spectrometer for measuring absolute differential cross sections for ion-induced electron emission from molecules

Nicolas Sens, Michal Ryszka, Jean-Christophe Poully, Alain Méry, Jean-Yves Chesnel, Violaine Vizcaino

A Velocity Map Imaging spectrometer for measuring absolute differential cross sections for ion-induced electron emission from molecules

N. Sens, M. Ryszka, J.-C. Poully, A. Méry, J.-Y. Chesnel and V. Vizcaino[1].

Centre de Recherche sur les Ions, les Matériaux et la Photonique (CIMAP) - UMR 6252 - Normandie Université, ENSICAEN, UNICAEN, CEA, CNRS, 14000 Caen, France

(Received XXXXX; accepted XXXXX; published online XXXXX)

In this paper, we present a newly developed crossed beam experimental set-up that utilizes the velocity map imaging (VMI) technique to measure simultaneously both kinetic energy and emission angle of electrons emitted from atoms or molecules upon ion collision. The projectile ion beam with keV to MeV kinetic energy crosses orthogonally the neutral target beam produced by an effusion cell. The emitted electrons are extracted and analyzed by a multi-electrode VMI spectrometer. By monitoring the target density, the projectile ion beam intensity and the beams' overlap, we are able to measure absolute differential cross sections for collision-induced electron emission from molecules. The characterization of the set-up and the methodology will be presented as well as first results for electron emission from uracil upon 0.98-MeV/u $^{12}C^{4+}$ collision.

I. INTRODUCTION

Electron emission following ion collisions with atoms or molecules has been studied for several decades. Electron emission from the target, projectile or both, electron transfer or electron interference have been the subject of numerous experimental and theoretical studies. Measuring the electron yield as a function of their kinetic energy allows a better understanding of the main ionization mechanisms, from soft collisions producing low energy electrons to binary collisions or inner-shell ionization producing well defined peaks at high energy. These fundamental collisional processes as well as experimental methods and theoretical descriptions are notably reviewed in the book written by N. Stolterfoht, R. D. DuBois and R. D. Rivarola [1] that gives a comprehensive overview of the research undertaken for the last 30 years of the 20th century.

In more recent years, ion collisions with biologically relevant molecules have received increasing interest due to applications to radiation biology. Absolute total or differential cross sections for electron emission have been measured and modeled for small biomolecules such as DNA/RNA nucleobases [2–11] and amino acids [12]. Experiments were mainly performed with bare ions such as protons [2–4,12], C^{6+} or O^{8+} [6,7] with a kinetic energy of a few MeV. The doubly differential cross sections for electron emission were found to be between 10^{-18} and 10^{-17} $cm^2.eV^{-1}.sr^{-1}$ at emission energies below 10 eV and to fall by roughly one or two orders of magnitude above 100 eV. Electron yields were measured using electrostatic analyzers (parallel plates or hemispherical) mounted on a turntable [2–7,12] and anchored to an absolute scale by normalization to other collisional processes (for which cross sections are known or measurable) such as Rutherford forward scattering [3,4], projectile elastic scattering at right angle [2] or Auger electron emission [6,7].

In this paper, we will present a different approach where absolute cross sections are directly estimated from the normalization of the number of emitted electrons N_{e^-} by the number of projectile ions N_P, the density ρ of the target beam, the detector efficiency ε and the length l of the collision volume due to the beams' overlap. Moreover, the electrons are detected using a Velocity Map Imaging (VMI) spectrometer that allows collecting, at once, electrons with different kinetic energies emitted in a solid angle of 4π steradians without the need to rotate an energy analyzer spectrometer. The electrode arrangement of the VMI spectrometer acts as an electrostatic lens which allows focusing particles with the same initial velocity vector into the same position on the detector regardless of their initial position (within a small volume (~20 mm^3) close to the center of the spectrometer). The velocity vector distribution of the emitted electrons is finally deduced from the image on the detector. This kind of spectrometer has been mainly used in combination with lasers or synchrotron radiation (VUV or soft X-rays) to analyze electrons from photoionization or photodetachment processes, and ionic fragments after photodissociation of gaseous targets [13–15]. It has also been used for low-energy electron–molecule collisions [16] in order to measure the kinetic energy of

[1] Corresponding Author : vizcaino@ganil.fr

dissociative electron attachment products. A special topic issue was recently published on developments and applications of velocity map imaging techniques [17]. To the best of our knowledge, the VMI technique has never been implemented for ion-induced electron emission.

In section II, the description and characterization of the experimental set-up as well as the methodology to obtain absolute cross sections are given. In section III, we will present the first results for absolute total and singly differential cross sections for electron emission from uracil upon ion collision (0.98-MeV/u $^{12}C^{4+}$).

II. DESCRIPTION OF THE EXPERIMENTAL SET-UP AND METHODOLOGY

A. General description of the experimental set-up

Each part of the experimental set-up will be described in detail in the following paragraphs. Here, only a brief description will be given. The projectile ion beam (keV to MeV ions) can be produced by a small source such as an ion gun, or by a large-scale accelerator such as the ones at GANIL in Caen (France). The set-up has been designed to be compact enough to be easily transported and coupled to a variety of beamlines. The ion beam is shaped by a series of slits before entering the collision chamber. Its intensity and position are monitored by a Faraday cup and an ion beam profiler, respectively, located after the collision chamber. The target beam is produced with a two-stage effusion cell and shaped by two consecutive skimmers before entering the collision chamber where it crosses orthogonally the projectile ion beam. A pneumatic push-pull shutter is placed between the two skimmers to block the target beam in order to measure the background (i.e. electrons from the residual gas) which is subtracted latter on. After crossing the collision chamber, a quartz crystal microbalance allows monitoring the mass flux of the target beam and thus obtaining the beam density. The electrons created in the collision region are extracted by a homemade multi-electrode VMI spectrometer and detected by a position sensitive detector constituted of two microchannel plates (MCPs) and a phosphor screen. The images are recorded with a camera: they represent the 2D projection of the electron cloud produced by the ionization of the target (see Figure). Therefore, by applying an inverse Abel transform we can reconstruct the velocity distribution (kinetic energy and emission angle) of the emitted electrons.

B. Methodology to determine absolute total and differential cross sections

Absolute cross sections σ (expressed in cm² in the following) can be determined by normalizing the count rate of detected electrons N_{e^-} (electrons.s^{-1}) by the detector efficiency ε, the count rate of projectile ions N_p (ions.s^{-1}), the density of the target beam ρ (molecules.cm^{-3}) and the

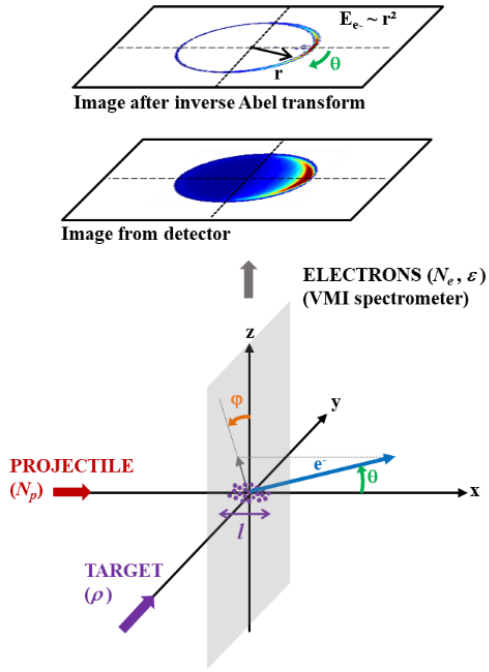

Figure 1: Definition of axes and emission angles θ (polar angle) and φ (azimuthal angle). Example of an image obtained for monoenergetic electrons emitted preferably in the forward direction (SIMION simulation) and its inverse Abel transform. The radius r gives information on the electrons energy ($E \sim r^2$, see energy calibration in Section E.2).

length of the interaction region l (cm): $\sigma = N_{e^-}/(\varepsilon\, N_p\, \rho\, l)$. The tools and methods to determine these different parameters are detailed in the following sections.

In order to study the kinetic energy (E) dependence and/or angular (Ω) dependence of electron emission, differential cross sections $d\sigma/dE$, $d\sigma/d\Omega$ or $d^2\sigma/dEd\Omega$ can be determined after analysis of the inverse Abel transform of the detector image. The inverse Abel transform numerically reconstructs a cylindrically symmetric 3D object (emitted electrons) from its 2D projection on a plane (detector) parallel the axis of symmetry (projectile ion beam). Electron emission has indeed a cylindrical symmetry along the projectile beam, which means that it does not depend on the azimuthal angle φ. The angular dependence of the cross section is usually expressed as a function of θ, the polar angle defined with respect to the projectile ion beam (see Figure for angle definition).

C. Characterization of the projectile ion beam

Details of the projectile ion beam section are shown in Figure 2. The projectile ion beam, from singly-charged keV ions to multiply-charged MeV ions, is cut down to a diameter of about 1 mm by two consecutive slits before going through the electrodes of the VMI spectrometer located in the collision chamber. The ion beam intensity,

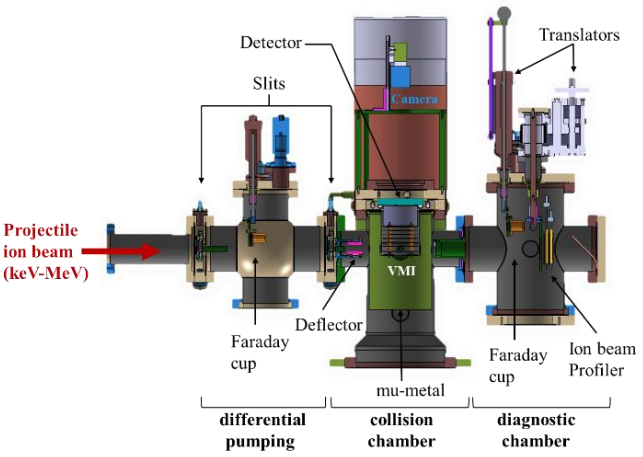

Figure 2: Schematic of the projectile ion beam part of the experimental set-up.

typically about 100 pA, is measured in the diagnostic chamber after the collision chamber, by means of a picoammeter (Keithley) connected to a cylindrical Faraday cup (length = 40 mm, diameter = 20 mm) with a 45° bottom to reduce backscattering. An electron repeller set at a negative voltage (for instance -200 V for ~ 1 MeV/u C^{4+}) is placed at the entrance of the Faraday cup to prevent secondary electrons to escape the Faraday cup and therefore to avoid overestimation of the ion beam intensity. The position of the Faraday cup can be adjusted vertically using a translator to compensate the small downwards ion beam deflection due to the electric field applied in the VMI spectrometer. This translator also allows the Faraday cup to be fully removed to use the ion beam profiler behind. The shape and position of the ion beam are monitored by this ion beam profiler, constituted of 47 horizontal and vertical wires spaced by 500 µm.

For low E/q ion beam (q being the charge of the ion), typically below 10 keV/q, the extraction field used to collect emitted electrons up to 200 eV can induce a downward deflection of the ion beam. At a distance of 340 mm downstream the interaction region, vertical profiles of a 4-keV He^+ beam are recorded with the ion beam profiler for different values of the extraction voltage, noted V_{ext}, which represents the potential difference between the interaction region and the front plate of the MCPs detector. In Figure, experimental measurements are compared to SIMION simulations. While the deflection is found to reach up to 11 mm on the profiler, the simulations indicate that it is less than 1 mm at the center of the interaction region (not shown here). However, to compensate this deflection and ensure a proper overlap in the interaction region, an electrostatic deflector (two 60 mm x 30 mm plates spaced by 16 mm) is placed before the entrance of the VMI spectrometer. As SIMION simulations are in very good agreement with the experimental data for the ion beam position at the profiler, they are also used to determine the voltages to apply on the deflector. These voltages depend on the extraction field

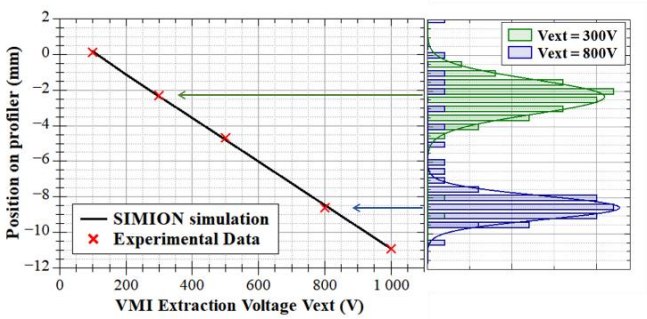

Figure 3: Comparison between SIMION simulations and experimental results for the position of a 4-keV He^+ ion beam on the profiler as a function of the extraction voltage applied to the VMI spectrometer. The right panel shows the vertical histograms of the profiler measured for the extraction voltages V_{ext} = 300 V and V_{ext} = 800 V. Gaussian functions have been fitted to these histograms to obtain the mean position.

used in the VMI spectrometer and on the projectile energy per charge unit, E/q. Typically, a few volts are necessary to straighten up keV ion beams in the interaction region.

D. Characterization of the target beam

In the experimental set-up, two types of target sources can be connected: a homemade supersonic jet source (see Figure) mainly used for calibration and characterization of the VMI spectrometer (Sections E.2 and E.3); and a two-stage commercial oven to produce an effusive beam of molecules (see Figure). For both configurations, the core of the target beam is selected by two consecutive skimmers separated by 75 mm. For the supersonic source the first skimmer is a 1 mm hyperbolic skimmer (Beam Dynamics) while a 3 mm conical skimmer is used for the effusive beam. In both cases, the second one is a 2 mm conical skimmer, mounted on a homemade zero-length gate valve used to isolate the target beam part from the rest of the set-up. In between the two skimmers, a pneumatic push-pull shutter is used to block the target beam during experiments and measure background electrons emitted in collisions with the residual gas.

The supersonic jet source is a ¼ inch stainless-steel tube with a laser-drilled hole at one end (Lenox laser). The source is mounted on a XYZ translator in order to optimize the alignment and the nozzle-skimmer distance (around 5 mm). Typically, we used a nozzle hole of 35 µm in diameter and expand about 6 Bar of rare gas (Ar or Kr) to get the best signal to noise ratio.

The oven is a two-stage effusion cell from Createc (DFC-40-10-Wk-SHM-Col) controlled with a DC-Power supply (PS-D700-EA). It is mounted on a DN40CF flange and water-cooled (Figure). It can handle temperatures up to 1500°C as it has been designed to evaporate metallic atoms. It has two independent cavities: the effusion cell (EC) in which the powder of molecules is inserted, and the hot lip (HL) which allows shaping the beam thanks to an aperture

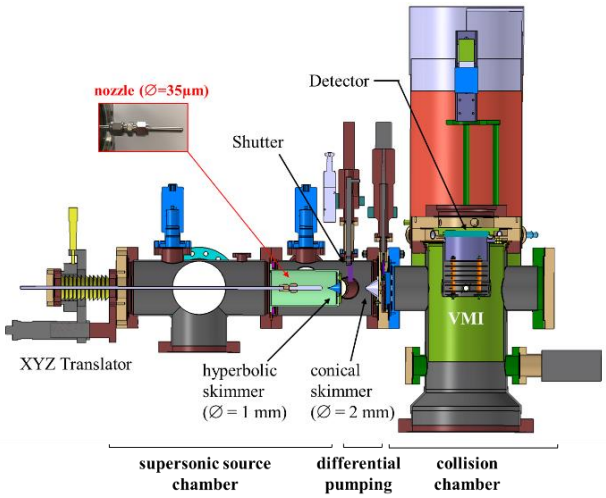

Figure 4: Supersonic jet source configuration for the target part of the experimental set-up

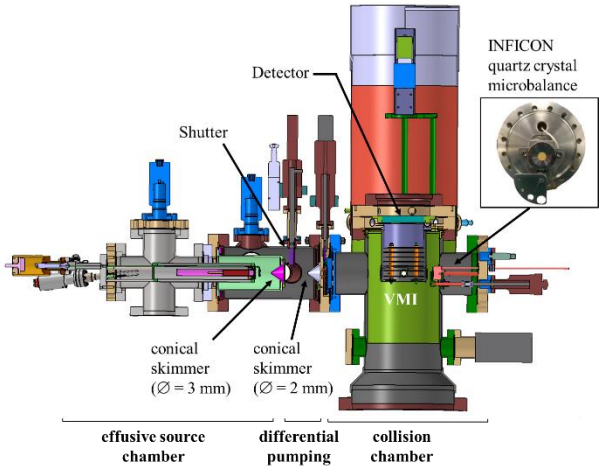

Figure 5: Effusive beam source configuration for the target part of the experimental set-up

tube (length = 30 mm, diameter = 3 mm). For biomolecules such as uracil or adenine, the EC is held at temperature of about 140°C while the HL is held at higher temperature to avoid condensation in the small exit aperture.

To determine the density ρ of the molecular beam created with the effusion cell, a water-cooled quartz crystal microbalance (model Inficon SL-B0E0) is placed behind the VMI spectrometer (see Figure) at 75 mm from the center of the interaction region. The sensor is a 8.2 mm diameter quartz crystal that oscillates at 5 MHz via the monitor (model Inficon STM-2). The mass deposition induces a reduction of the oscillating frequency, which gives back the mass flux Φ in µg.cm^{-2}.s^{-1}. From this value, knowing the velocity distribution of the beam, one can deduce the mass density in µg.cm^{-3} or rather the density ρ in molecules.cm^{-3} at the quartz crystal microbalance. The velocity distribution *f(v)* of the molecular beam is derived from the Maxwell-

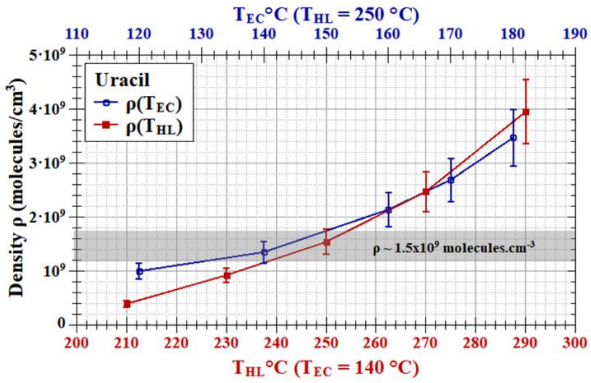

Figure 6: Evolution of uracil density as a function of oven temperatures T_{EC} (blue open circle) and T_{HL} (red full square). The uncertainty is estimated to be around 19% and takes into account both systematic errors on the estimation of the length l ($\Delta l/l$ ~ 9%) and the temperature T ($\Delta T/T$ ~ 4%) and statistical errors on the measure of the mass flux Φ by the quartz crystal microbalance ($\Delta\Phi/\Phi$ < 5% where $\Delta\Phi$ is the standard deviation).

Boltzmann distribution as $f(v) = 2(m/2kT)^2\, v^3\, e^{-mv^2/2kT}$ with m the mass of the molecule, T the temperature ($T = T_{HL}$) and k the Boltzmann constant [18]. The mean density is then determined by integrating over that velocity distribution. Taking into account the divergence of the beam known from the position and sizes of the different apertures along the beam path, the target density in the collision volume can be deduced. It is found to be typically around 1.5x10^9 molecules.cm^{-3}. To increase the beam density one can rise the oven temperatures T_{EC} and/or T_{HL} (see Figure) but it also increases the risk of thermal decomposition of the molecule. In order to define the critical temperatures to use, thermal decomposition has been studied with the use of a quadrupole mass spectrometer (QMS, Balzers Prisma) mounted temporarily at the position of the quartz crystal microbalance. We have monitored the modification of the mass spectra due to electron impact ionization in the QMS and in particular, the apparition of new fragmentation channels or new species as the oven temperature increases. For uracil, we found that the T_{EC} should not exceed 140°C while T_{HL} can reach up to 250°C.

The knowledge of the diameter of the beam in the interaction region (which is also the length l of the collision volume, see Figure) is necessary for the determination of the target density and later on the absolute cross section. It has been determined using small apertures of respective area of 5 mm², 10 mm², 20 mm², 35 mm² and 52.8 mm² placed in front of the quartz crystal microbalance (see the insert in Figure). We found that the beam density is not uniform on its section (higher density in the center part of the beam), which is consistent with the effusive character of the beam formed in the aperture tube [18]. In the present case, we found that 85% of the beam is contained in the 20-mm² section and 100% of the beam in the 35-mm² section.

Therefore, we have estimated the beam diameter to be of about 6.7 mm at the quartz crystal microbalance, which corresponds to a size of 5.4 mm in the interaction region taking into account the divergence of the beam. An uncertainty of Δl = 0.5 mm is associated with this value.

E. The Velocity Map Imaging Spectrometer

1. Description

We have designed a compact multi-electrode VMI spectrometer in order to detect electrons with kinetic energy up to 200 eV. The use of a multi-electrode spectrometer allows having a reasonably good energy resolution (see section E.3 for further details) despite its short length. The trajectories of low energy electrons being quite sensitive to magnetic field, the VMI spectrometer is shielded from the Earth magnetic field and other magnetic sources by μ-metal cylinders placed both inside and outside the collision vacuum chamber. Effects of the magnetic field on the spectrometer energy resolution are discussed in section E.3.

Figure shows a schematic of the home-built VMI spectrometer. It has a total length of 114 mm. It is constituted of 6 planar electrodes and a cylindrical electrode. All the planar electrodes have an outer diameter (OD) of 80 mm, a thickness of 1 mm and are spaced by 8 mm except the first two (V_0 and V_1) which are spaced by 10 mm. The first one (V_0) is a plain electrode and the five others have an increasing inner diameter (ID) from 40 to 56 mm. The cylindrical electrode is a 48 mm long tube (OD = 80 mm, ID = 76 mm) with an opening of 60 mm at the entrance and is 8 mm above the last thin electrode. This electrode assembly fits inside a tube (OD = 88 mm, ID = 86 mm) acting as an electrostatic shield and is mounted on a customized DN-150-CF flange. The detector (2 MCPs + phosphor screen) is mounted on a separate DN-150-CF flange and the front plate of the MCPs sits 2 mm above the cylindrical electrode when assembled.

Voltages are applied directly on the outer tube (V_{shield}), the first three planar electrodes (V_0, V_1 and V_f) and the cylindrical electrode (V_t). They are applied on the three middle electrodes via a resistance bridge voltage divider (R = 1.8 MΩ). The front side of the MCP is polarized at the same voltage as the cylindrical electrode (V_t). In standard operation, V_0 and V_1 are set to the same value. The more positive voltages (V_f and V_t) applied to the upper electrodes create a weak inhomogeneous electric field to focus emitted electrons on the detector. The potential at the center of the collision region is thus very close to V_0. As mentioned earlier, the potential difference between V_t and V_0 defines the extraction voltage (noted V_{ext}) and therefore the energy range of the detectable electrons.

V_{shield}, V_0 and V_1 are set at a negative potential to avoid electrons created outside the VMI spectrometer to enter and reach the detector. The potential to apply depends on the

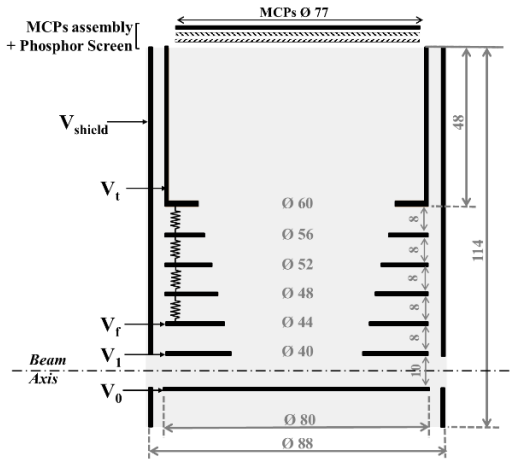

Figure 7: Schematics of the multi-electrode Velocity Map Imaging spectrometer. All dimensions are in mm.

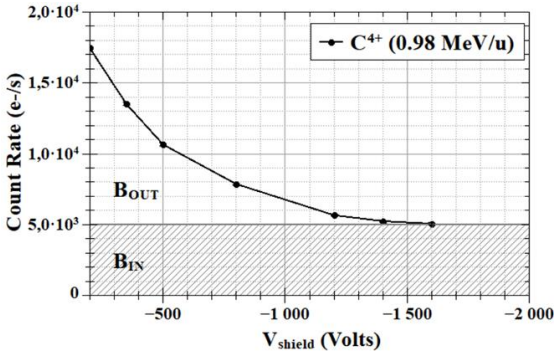

Figure 8: Count Rate of background signal (i.e. electron emission from residual gas) as a function of the potential applied to V_{shield} (= V_0 = V_1) for the projectile C^{4+} ion beam at 0.98-MeV/u kinetic energy. The measurement is performed for the VMI extraction V_{ext} = 1000V.

kinetic energy of the ion beam. To remove this background signal (noted B_{OUT}), a bias potential up to -2000 V for MeV ion beams is necessary (Figure) while only -200 V is enough for keV beams (not shown). A non-negligible amount of electrons due to ionization of the residual gas inside the VMI spectrometer still reaches the detector. To reduce this second background contribution (noted B_{IN}), the electrode V_1 can be set at a slightly lower potential than the electrode V_0 ($V_1 = V_0 - dV$). The electric field created by this potential difference dV reduces the amount of electrons created along the track of the ion beam to be detected as they are pushed towards V_0 while the one coming from the collision region (i.e. center of the VMI spectrometer) are less affected and reach the detector. However, this potential does change the electric field in the interaction region and one has to adjust V_f to ensure that the electrons coming from the collision between the projectile and the target are still well focused onto the detector. Applying the potential difference dV is useful when the target beam is not so well collimated and

target molecules are scattered in the VMI spectrometer and contribute to B_{IN}. However, this contribution is negligible for the biomolecules we have studied (adenine and uracil), most of electrons coming from interaction outside the small collision volume being due to ionization of the residual gas (N_2, H_2O) rather than scattered target molecules. It is then possible to remove this contribution by measuring alternatively the electron signal with ($S+B_{IN}$) and without the target beam (B_{IN}) with the use of the pneumatic push-pull shutter and by subtracting B_{IN}. In standard operation ($\rho \sim 1.5x10^9$ molecules.cm^{-3} and a base pressure in the low 10^{-8} mbar in the collision chamber), the ratio S/B_{IN} is typically around 0.5.

The detector from Hamamatsu is constituted of two 80 mm microchannel plates (effective diameter = 77 mm, see Figure) in chevron configuration and a phosphor screen (P43) mounted on DN-150-CF (Ref F2226-21PF252). The MCPs have 25-µm pore size with 31-µm center-to-center spacing giving a maximum detection efficiency of about 60%. However, the detection efficiency ε depends also on the energy of the electrons. The energy dependence curve used is the one from the constructor manual that refers to a study by Galanti *et al.* [19]. It presents a maximum for electrons of about 300 - 400 eV. In our case, low energy emitted electrons are accelerated in the VMI spectrometer by the potential difference V_{ext} and therefore in first approximation $E \sim qV_{ext}$ with q the elementary charge. A potential difference of 2160 V is applied between the two microchannel plates and a difference of 3000 V between the rear side of the MCPs assembly and the phosphor screen (Photek DPS3 power supply).

The CMOS camera (JAI GO-2400M-USB) coupled to a high-resolution lens (Kowa LM25HC) is situated around 30 cm above the detector. The 8-bits monochromatic camera has 1216 x 1216 pixels sensor; each pixel images an area of 69 x 69 µm on the phosphor screen. The camera can also be used in lower resolution mode with a binning of 608 by 608 pixels.

The count rate (N_{e^-}, electrons.s^{-1}) is measured at the rear side of the MCPs with a use of a preamplifier and discriminator. The raw images of the detector are recorded and averaged to get the spatial distribution of the electron impacts on the detector, which gives access to the kinetic energy and angular distribution of the emitted electrons. The averaged image is then normalized by the MCPs count rate. Another method would have been to directly count the number of spots on the images of the detector to get simultaneously the number of electrons and their position. With that method, we would have to use an exposure time of the camera larger than the decay time of the phosphor screen (τ = 3ms) to properly estimate the number of spots per image. However, an exposure time of about 5 to 10 ms would imply a larger number of spots per image and a risk of missing overlapping spots at the center of the detector, even when working with very low count rate. Therefore, the use of the averaged raw images normalized by the MCPs count rate was found to be more reliable and this method was chosen for the determination of absolute ion-induced electron emission cross sections from uracil presented in Section III.

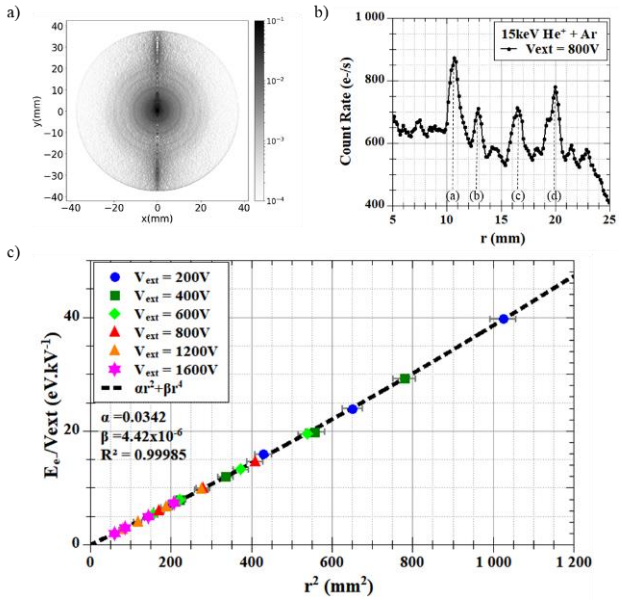

Figure 9 : a) Inverse Abel transform of emitted electrons from the collision system 15-keV He^+ + Ar detected with extraction voltage V_{ext} = 800 V. b) Radial distribution after angular integration of the inverse Abel transform. c) Calibration curve (i.e. E/Vext as a function of r²) of the VMI spectrometer, obtained from the radial coordinates r of the Auger electrons (with energies E of 3.3 eV, 4.8 eV, 7.95 eV and 11.7 eV) from the collision system 15-keV He^+ + Ar, and measured for six different extraction voltages V_{ext} ranging from 200 V to 1600 V.

2. Energy Calibration

The square of the radial coordinate (r²) of the electron spot on the detector's processed image, i.e. after inverse Abel transform, is proportional to the ratio E/V_{ext}, with E the kinetic energy of the detected electron and V_{ext} the extraction potential applied to the VMI spectrometer ($E/V_{ext} = \alpha\ r^2$). The α parameter is characteristic of the VMI spectrometer, in particular of its length and the focusing lens arrangement.

In order to determine experimentally the calibration parameter α, we used the collision system 15-keV He^+ on Ar. The Ar beam was formed via a supersonic expansion of 5 Bar of pure argon (99.9999 %, Air Liquide) through a 35 µm nozzle and shaped by two skimmers (1 mm and 2 mm of diameter) before reaching the collision chamber. The collision system 15-keV He^+ + Ar has been studied a few decades ago [20,21] and the electron spectra show a series of sharp peaks at defined energies assigned to autoionization from metastable states of Ar^{+*} after electron

capture from the projectile. To calibrate our system we used the peaks at 3.3 eV, 4.8 eV, 7.95 eV and 11.70 eV assigned respectively to the following autoionisation transitions [20,21]:

$Ar^+ 3s^1 3p^5(^1P)4s(^2P) \rightarrow Ar^{2+} 3s^2 3p^4 (^1D)$ (a)
$Ar^+ 3s^1 3p^5(^1P)4s(^2P) \rightarrow Ar^{2+} 3s^2 3p^4 (^3P)$ (b)
$Ar^+ 3s^1 3p^5(^1P)4p(^2P) \rightarrow Ar^{2+} 3s^2 3p^4 (^1D)$ (c)
$Ar^+ 3s^1 3p^5 3d \rightarrow Ar^{2+} 3s^2 3p^4$ (d)

We have recorded the electron yield for different extraction voltages V_{ext} ranging from 200 V to 1600 V. The higher the extraction voltage the smaller the ring corresponding to a defined electron energy on the detector. After angular integration of these images, we obtain the radial distribution of the detected electrons (see an example for V_{ext} = 800V, Figure b). We can therefore obtain, for each extraction field, the corresponding position r(mm) of the different Auger energy peaks (a, b, c and d) and build the calibration curve (see Figure c). The experimental points deviate slightly from the theoretical $E/V_{ext} = \alpha\, r^2$ curve. Therefore, the data were fitted by a quadratic polynomial on r^2, i.e. $E/V_{ext} = \alpha\, r^2 + \beta\, r^4$ with a very good agreement (R^2 = 0.99985). The discrepancy from theory is not yet fully explained but we have ruled out the possibility of a deformation of the image by the camera. It could be due, however, to a small deviation from the ideal extraction field.

3. Energy resolution

In a VMI spectrometer the radial ($\Delta r/r$) or energy ($\Delta E/E = 2\,\Delta r/r$) resolution is not constant over the whole range, i.e. peaks corresponding to electrons of a given energy are more or less resolved depending on the extraction voltage and thus, depending on their position on the detector. Apart from the intrinsic properties of the spectrometer (length, electrode arrangement, applied voltages), other factors, such as the camera resolution, the size of the interaction region (beams overlap), the presence of a weak stray magnetic field or the size of the electron cascade spot on the phosphor screen, can have an impact on the resolution. SIMION simulations have been performed to quantify these different contributions to the energy resolution. In the simulations, groups of 10^6 electrons with energy from 0.1 eV to 40 eV are emitted isotropically in a 4π solid angle and extracted with V_{ext} = 1000 V. Images from the simulation are pixelated to match the camera resolution (608 x 608 or 1612 x 1612) before performing the inverse Abel transform using the same method as for experimental data. After angular integration of the transformed image, the full width at half maximum (FWHM) noted Δr for a peak at the position r is measured in order to plot the radial resolution $\Delta r/r$ as a function of r.

The contribution of the size of the interaction volume has been studied by running simulations using a cylindrical volume of adjustable radius *a* and length *l*. Figure 10a shows that mainly the resolution at the center and the edge of the detector is affected when compared with an ideal point source. It shows the limit of the capability of our VMI spectrometer to focus electrons with same velocity vector onto the detector when created at an initial position far from the center. To minimize this effect both the projectile and target beams are shaped to a minimum size with the help of slits and skimmers, respectively. Typically, the collision volume is a cylinder of radius *a* = 1 mm and length *l* ~ 5-6 mm (see Section II.D).

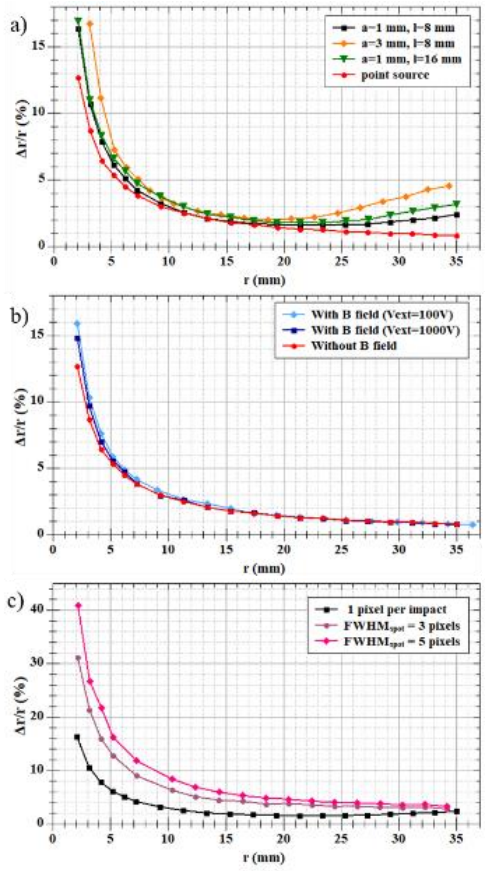

Figure 10: SIMION simulated radial resolution $\Delta r/r$ (%) as a function of radius r (mm). For all plots, images from the simulation are pixelated with 608x608 pixels to match the camera resolution. a) Effect of the collision volume: simulations are performed with electrons from 0.1 eV to 40 eV at V_{ext} = 1000 V for three types of cylindrical collision volume (of radius *a* and length *l*) and compared to the case of a point source (red plot). b) Effect of the magnetic field: simulations are performed with electrons from 0.1 eV to 40 eV at V_{ext} = 1000 V and with electrons from 0.01 eV to 4 eV at V_{ext} = 100 V. The collision volume is considered as a point source. The B_z component of the measured magnetic field is implemented in the simulation. c) Effect of the spot size on the phosphor screen: the pixelated image (608 x 608) from the SIMION simulation performed for a cylindrical collision volume (a=1mm, l=8mm) and including the B_z component of the measured magnetic field is convoluted by a 2D Gaussian with FWHM = 3 pixels and 5 pixels before applying the inverse Abel transform.

Low energy electrons are also affected by stray magnetic field. Despite µ-metal shielding, the remaining magnetic field can modify their trajectories and therefore affect the resolution. We have measured experimentally the magnetic field inside the VMI spectrometer along the z axis and in the (xy) plane of the interaction region using a Hall effect magnetic probe (x and y are the propagation axes of the projectile and target beam respectively and z is the spectrometer axis, see Figure). The component $\mathbf{B_x}$ and $\mathbf{B_y}$ of the magnetic field are negligible (< 1 µT) in the VMI spectrometer. The component Bz along the spectrometer axis is around 5 µT at the collision region and increases up to 30 µT in the front plate of the MCPs due to the opening of the µ-metal shielding. Experimental values of the B field are incorporated in the simulation (Figure b) which were performed with electrons from 0.1 eV to 40 eV at V_{ext} = 1000 V and with electrons from 0.01 eV to 4 eV at V_{ext} = 100 V. The resolution is slightly worse for radius below 6–7 mm for V_{ext} = 1000 V and below 17–19 mm for V_{ext} = 100 V which corresponds to an electron energy of about 1.5 eV. This simulation was done for an ideal point source, if a cylindrical collision region (a = 1 mm and l ~ 5–6 mm) is considered, the effect of B field on the resolution becomes negligible.

Another important factor that can worsen the resolution is the spot size on the phosphor screen when using the raw image from the detector instead of determining the centroid for each spot and thus reducing the spot to one pixel. The average diameter of a spot has been estimated experimentally to be about ~ 3 pixels in case the camera resolution is set at 608 x 608 pixels (i.e. ~400 µm). To take into account the size of the spot, the pixelated image resulting from the SIMION simulation is convoluted by a 2D-gaussian with FWHM of n pixels (n=3 and n=5 in Figure c) before applying the inverse Abel transform and angular integration. As expected, the effect of the spot size on the relative resolution Δr/r is more significant for the smallest radii r for which a lower number of pixels are available. For example, at r < 10 mm, the resolution is worsen by a factor of ~ 2 for 3-pixel spots compared to the ideal case of point-like spots. However, Δr/r remains lower than 12% for radii ranging from 5 to 35 mm.

Experimentally, we have determined the resolution of the spectrometer by measuring the FWHM (Δr) of the peaks corresponding to the photoelectrons of krypton (6.55 eV and 7.22 eV) upon He I photoionization (Photon energy $E\varphi$ = 21.22 eV) with an UV lamp (Figure).We have used Kr photoelectrons rather than Auger electrons from Ar upon 15-keV He^+ impact (see Energy calibration, Section E2) to have electron spectra without the continuum electrons emission,

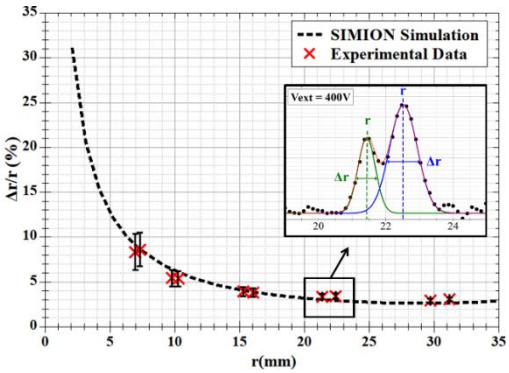

Figure 11: Experimental radial resolution Δr/r (%) as a function of radius r (mm). The FWHM is measured for both peaks corresponding to $^2P_{1/2}$ and $^2P_{3/2}$ photoelectrons of Krypton for V_{ext} ranging from 150V to 3000V (see insert for V_{ext} = 400V). Experimental data are compared to SIMION simulations (black dotted line) performed with a cylindrical collision volume (r = 1mm, l = 6 mm), with the B_z component of the experimental magnetic field, 608x608 pixels camera binning and a simulated spot size on the phosphor screen of 3 pixels.

and thus, to facilitate the fitting procedure and determination of the resolution. The Kr beam was formed via a supersonic expansion of 6 Bar of krypton through the 35 µm nozzle. A collision volume of parameters a = 1 mm and l = 7 mm is used[2]. Experiments are performed for extraction from V_{ext} = 150 V to V_{ext} = 3000 V in order to cover a wide surface of the detector (from r ~ 7 mm to r ~ 30 mm). These measurements were done in typical experimental conditions (same condition as in Section III) but not necessarily in conditions were the best resolution can be achieved. Indeed, the camera resolution was set at 608 x 608 pixels (rather than 1216 x 1216 pixels), and the raw images were used (i.e. no reduction of the spot to its centroid). SIMION simulations, performed with these experimental conditions, reproduce very well the experimental data indicating that the different factors playing a role in the resolution are well identified and understood. Knowing the resolution of the VMI spectrometer and the contribution of the factors involved is necessary, especially when studying a system with well-defined peaks due to Auger processes for example. It is then possible to choose the right parameters to record resolution-optimized electron spectra and/or to deconvolute the measured signal by the known resolution if necessary. Depending on the electrons energy, one can adjust the extraction voltage V_{ext} so that the position of their impact on the detector is far from its center or its edge where the resolution is worsen either by the spot size on the phosphor screen or by the volume of the interaction region. Hence, in the following section dedicated to the measurement of

[2] For this system, the collision volume cannot be determined using the ion beam profiler and quartz crystal microbalance. Therefore, it has been imaged by detecting Kr^+ photo ions formed in the interaction region with a homogeneous extraction field applied to the spectrometer. In principle, this technique could also be used in the case of ions/molecules collisions to determine more accurately the beams overlapping volume if we were able to image only the parent ions (selected by time-of-flight for instance) and not the molecular fragments that distort the image due to kinetic energy release.

absolute cross sections for electron emission from uracil, by considering only electrons for which the radial coordinate r is between 5 mm and 35 mm, we provide data with a relative resolution Δr/r that is lower than 12%.

III. ABSOLUTE CROSS SECTION FOR ELECTRON EMISSION FROM URACIL UPON 0.98-MeV/u $^{12}C^{4+}$ COLLISION

First results with this new experimental set-up are the determination of absolute cross sections for electron emission from the nucleobase uracil ($C_4H_4N_2O_2$) upon interaction with a carbon ion beam ($^{12}C^{4+}$) at 0.98 MeV/u. Measurements were performed for different extraction voltages (V_{ext} from 250 V to 2200 V) in order to cover a wide energy range of the emitted electrons (0.2 eV to 100 eV) and to validate the methodology. On average, the uracil beam density was around 1.15x10^9 molecules.cm^{-3} and the ion beam intensity of about 130 pA, i.e. 2x10^8 ions.s^{-1}. For each extraction voltage, at least 10^5 images of the detector (images with 608 x 608 pixels) were taken with the exposure time of the camera being set between 1 and 5 ms depending on the extraction voltage.

The absolute single differential cross sections as a function of electron energy (SDCS(E), i.e. $d\sigma/dE$(E)) measured for the different extraction voltages V_{ext} are shown superimposed in Figure. The average of the SDCS(E) (black curve) is also determined and shifted by a factor 5 to ease the reading of the figure. The cross section shows a maximum at low energy (around 1 eV) and then decreases by a factor ~30 at 100 eV. Electrons with energy $E > \alpha.r_{MCP}^2.V_{ext}$ can reach the detector if emitted towards it and therefore modify the overall shape of the energy distribution. However, as most of the emitted electrons have rather low energy (below 10eV), the effect of these higher energy electrons has been found rather negligible (SIMION simulation), even at the lowest extraction voltage V_{ext} = 250 V. This is also confirmed experimentally with the good superposition of the four SCDS(E) in Figure.

The uncertainty on each SDCS(E) values varies between 25% and 30%. It is determined as the quadratic sum of the statistical error $\Delta\sigma_{stat}$ and systematic error $\Delta\sigma_{syst}$. Statistical error $\Delta\sigma_{stat}$ represents fluctuations on the measure of the number of emitted electrons N_{e^-} ($(\Delta N_e)_{stat} = \sqrt{N_e}$), of the number of projectile ions N_P ($(\Delta N_P/N_P)_{stat} = \Delta I/I$ where I is the ion beam current measured by the Faraday cup and ΔI the standard deviation) and of the density ρ ($(\Delta\rho/\rho)_{stat} = \Delta\Phi/\Phi$ where Φ is the mass flux measured by the quartz crystal microbalance and ΔΦ the standard deviation). It is between 5% and 10% depending on the experimental conditions. Systematic error $\Delta\sigma s_{yst}$ is more difficult to determine accurately. In the present case, we have estimated it to be around 23% and to be due to the uncertainty on the determination of the target beam density ρ ($(\Delta\rho/\rho)_{syst}$ ~ 19%), the size of the interaction region l ($(\Delta l/l)_{syst}$ ~ 9%), the

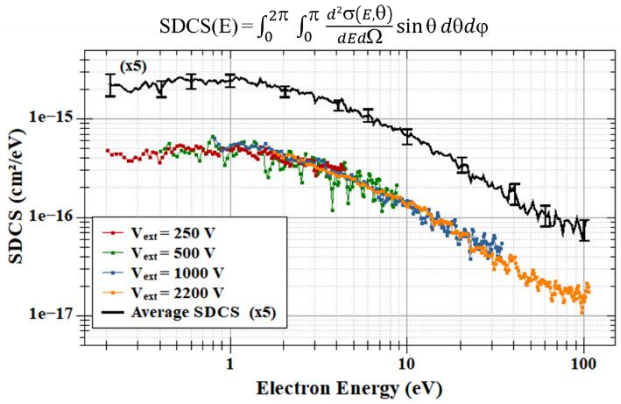

Figure 12: Absolute single differential cross section SDCS(E) for electron emission from uracil upon 0.98-MeV/u $^{12}C^{4+}$ collision. SDCS(E) in cm²/eV determined for four VMI extraction voltages (V_{ext} = 250 V, 1000 V, 2200 V and 4000 V) are shown as well as the average SDCS(E) multiplied by a factor 5 (for graphical reasons) and its associated uncertainties.

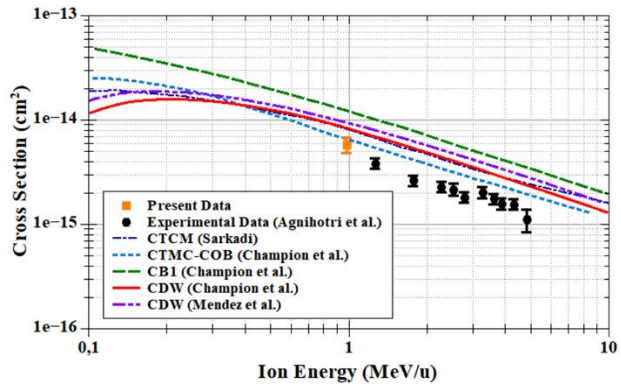

Figure 13: Absolute cross section for electron emission from uracil upon 0.98-MeV/u $^{12}C^{4+}$ collision integrated between 0.2 eV to 100 eV (orange square). The present data is compared to experimental data from Agnihotri et al.[5] as well as several theoretical results [8,11,22].

detector efficiency ε ($(\Delta\varepsilon/\varepsilon)_{syst}$ ~ 10%). The systematic errors due to the determination of N_{e^-} (MCP acquisition chain), N_P (Faraday cup) or electron energy distribution (Abel transform) are assumed to be negligible. The resultant uncertainty on the average SDCS(E) is show in Figure for a few electron energies to ease the plot: it varies between 10% and 30% depending on the number of overlapping SDCS measurements.

Integral cross section (ICS) between 0.2 eV and 100 eV is estimated to be around 5.79 ± 1.03 x10^{-15} cm². In Figure, we compare our value to both experimental [5] and theoretical cross sections [5,8,11,22] from the literature. The experimental cross sections from Agnihotri *et al.* [5] are determined by integrating time-of-flight (ionization and fragmentation) spectra of uracil and then put on an absolute scale using a different experimental set-up where electron

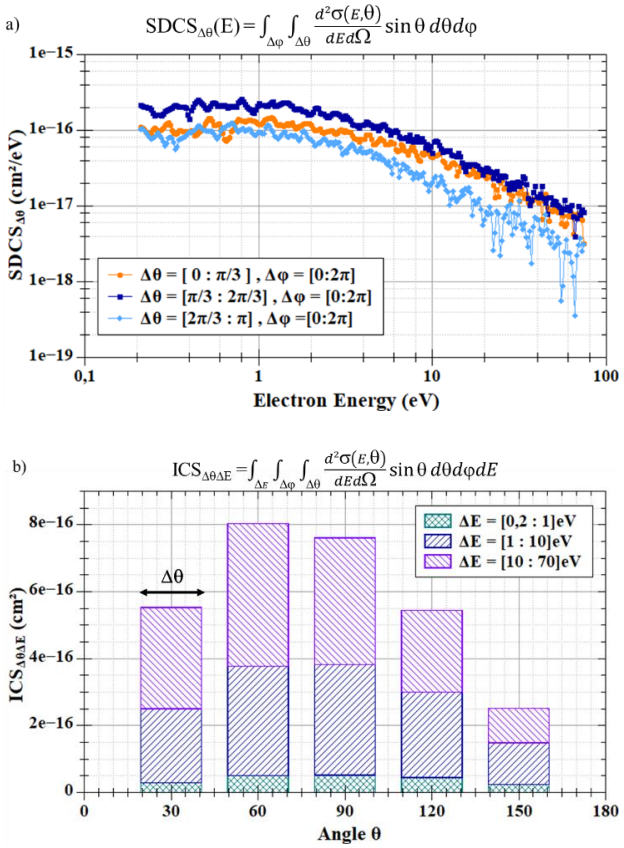

Figure 14: a) Absolute single differential cross section $SDCS_{\Delta\theta}(E)$ in cm²/eV for electron emission from uracil upon 0.98-MeV/u $^{12}C^{4+}$ collision determined for three different angular ranges Δθ : [0 : π/3], [2π/3 : π] and [π/3 : 2π/3]. b) Absolute integral cross sections $ICS_{\Delta\theta,\Delta E}$ in cm² determined for different angular ranges Δθ and energy ranges ΔE (Δφ = [0 : 2π]).

emission doubly differential cross sections ($d^2\sigma/dEd\theta(E,\theta)$) measured in the energy range [6-600eV] and angular range [30° - 135°] are integrated (see [5,6] for more details). The theoretical models are either classical ones such as the Classical Trajectory Monte Carlo model (CTCM) [19] with the classical over the-barrier description (CTCM-COB) [8] and quantum mechanics ones such as continuum distorted wave-eikonal initial state (CDW) [8,11] or first Born approximation (CB1) [8] models. In most cases, the molecule is treated as the sum of its constituent atoms [8,11]. The different computed CS are quite similar in this ion energy range but tend to differ below 0,1 MeV/u (not shown here) when the ion velocity gets close to the bound electron velocity. As the SDCS(E) drops significantly for high-energy electrons [6], our measurement gives a value in reasonably good agreement with both theory and experimental data, despite the restricted energy range ([0.2 - 100] eV) considered here.

To study the angular dependence of the electron emission, one can plot the absolute doubly differential cross sections DDCS(E,θ) i.e. $d^2\sigma/dEd\Omega(E,\theta)$ that can be deduced directly from the inverse Abel transform of the detector images. However, due to the poor statistics, we rather plot here the absolute SDCS(E) integrated on a specific angular range Δθ, noted $SDCS_{\Delta\theta}(E)$. In Figure a, the $SDCS_{\Delta\theta}(E)$ are determined for three angular ranges Δθ to highlight the forward emission [0 : π/3], backward emission [2π/3:π] and orthogonal emission [π/3 : 2π/3]. Each $SDCS_{\Delta\theta}(E)$ corresponds to the average of the measurements performed for the different VMI extraction voltages V_{ext} (from 250 V to 2200 V) as in Figure. In this figure, we can see that below 1eV, the forward and backward emission are roughly of the same magnitude. Between 1 eV and 10 eV, we observe a break of the forward/backward symmetry as the forward emission increases to reach the orthogonal emission magnitude above 10 eV. This increase of forward emission is characteristic of two-center electron emission where ejected electrons are attracted by the outgoing projectile ions.

Another way to observe and quantify both the energy and angular dependence in ion-induced electron emission processes is to plot the integral cross section $ICS_{\Delta\theta,\Delta E}$ for specific angular ranges Δθ and energy range ΔE (Figure b). In this case, we have integrated over smaller angular ranges Δθ = θ ± 10° with θ from 30° to 150° with 30° step and for 3 energy ranges ΔE ([0.2 eV : 1 eV], [1 eV : 10 eV] and [10 eV : 70 eV]). From this figure we can see that low energy electrons (below 10eV) contribute almost to half of the $ICS_{\Delta\theta,\Delta E}$. Concerning the angular dependence of the electron emission, an isotropic emission should manifest with a symmetry of the $ICS_{\Delta\theta,\Delta E}$ with respect to the angle θ = 90° (due to the sin θ). While it is almost the case for very low energy electrons (below 1eV), as the electron energy increases the forward/backward asymmetry increases which indicates a dominance of two-center electron emission over soft collisions in which the minimum projectile-target distance is (significantly) larger than one atomic unit.

IV. CONCLUSION AND OUTLOOK

In this contribution, we have described the new experimental set-up that will be used to determine absolute cross section for ion-induced electron emission from molecules. Electron emission is measured with the use of a compact multi-electrode velocity map imaging spectrometer giving access to both kinetic energy and emission angle at once. The advantage of this technique compared to conventional electrostatic (parallel plate or hemispherical) analyzer is the possibility to access to sub-eV electrons and to a wider emission angle range. The methodology to get absolute cross section is based on the determination of each parameter (N_e-, the number of electrons per time unit, N_p the number of projectiles per time unit, ε the detector efficiency, ρ the density of the target and l the length of the collision volume) rather than

using typical normalization techniques. The first results obtained for the nucleobase uracil are in good agreement with the experimental and theoretical values from the literature and validate our methodology. More experiments are planned in the near future to investigate electron emission dependence on both the projectile ion energy and charge state. Moreover, a new target source for the production of a metallic nanoparticle beam is currently under commissioning. This source, constituted of a nebulizer and an aerodynamic lens, will then be coupled to the VMI spectrometer to perform a systematic study of the electron emission cross sections as a function of the nanoparticle's size (50 nm to 100 nm) and/or material (Au, Ag, Pt). Indeed, we aim to shed light on the radiosensitizing effect of metallic nanoparticles as the ion-induced electron emission is thought to be in part responsible for local dose enhancement in ion beam therapy.

AKNOWLEDGEMENT

The authors acknowledge the support of the Agence Nationale de la Recherche (ANR), under grant ANR-16-CE30-0006. N. Sens acknowledges the Normandy Regional Council for his PhD grant.

REFERENCES

[1] N. Stolterfoht, R. D. DuBois, and R. D. Rivarola, *Electron Emission in Heavy Ion-Atom Collisions* (Springer, Berlin ; New York, 1997).

[2] P. Moretto-Capelle and A. Le Padellec, *Electron Spectroscopy in Proton Collisions with Dry Gas-Phase Uracil Base*, Phys. Rev. A **74**, (2006).

[3] Y. Iriki, Y. Kikuchi, M. Imai, and A. Itoh, *Proton-Impact Ionization Cross Sections of Adenine Measured at 0.5 and 2.0 MeV by Electron Spectroscopy*, Phys. Rev. A **84**, 052719 (2011).

[4] A. Itoh, Y. Iriki, M. Imai, C. Champion, and R. D. Rivarola, *Cross Sections for Ionization of Uracil by MeV-Energy-Proton Impact*, Phys. Rev. A **88**, 052711 (2013).

[5] A. N. Agnihotri, S. Kasthurirangan, S. Nandi, A. Kumar, M. E. Galassi, R. D. Rivarola, O. Fojón, C. Champion, J. Hanssen, H. Lekadir, P. F. Weck, and L. C. Tribedi, *Ionization of Uracil in Collisions with Highly Charged Carbon and Oxygen Ions of Energy 100 KeV to 78 MeV*, Phys. Rev. A **85**, 032711 (2012).

[6] A. N. Agnihotri, S. Nandi, S. Kasthurirangan, A. Kumar, M. E. Galassi, R. D. Rivarola, C. Champion, and L. C. Tribedi, *Doubly Differential Distribution of Electron Emission in Ionization of Uracil in Collisions with 3.5-MeV/u Bare C Ions*, Phys. Rev. A **87**, 032716 (2013).

[7] S. Bhattacharjee, C. Bagdia, M. R. Chowdhury, A. Mandal, J. M. Monti, R. D. Rivarola, and L. C. Tribedi, *Bare-Carbon-Ion-Impact Electron Emission from Adenine Molecules: Differential and Total Cross-Section Measurements*, Phys. Rev. A **100**, 012703 (2019).

[8] C. Champion, M. E. Galassi, O. Fojón, H. Lekadir, J. Hanssen, R. D. Rivarola, P. F. Weck, A. N. Agnihotri, S. Nandi, and L. C. Tribedi, *Ionization of RNA-Uracil by Highly Charged Carbon Ions*, J. Phys.: Conf. Ser. **373**, 012004 (2012).

[9] C. Champion, M. E. Galassi, P. F. Weck, S. Incerti, R. D. Rivarola, O. Fojón, J. Hanssen, Y. Iriki, and A. Itoh, *Proton-Induced Ionization of Isolated Uracil Molecules: A Theory/Experiment Confrontation*, Nuclear Instruments and Methods in Physics Research Section B: Beam Interactions with Materials and Atoms **314**, 66 (2013).

[10] C. Champion, M. E. Galassi, P. F. Weck, C. Abdallah, Z. Francis, M. A. Quinto, O. Fojón, R. D. Rivarola, J. Hanssen, Y. Iriki, and A. Itoh, *Ionization Induced by Protons on Isolated Molecules of Adenine: Theory, Modelling and Experiment*, J. Phys.: Conf. Ser. **488**, 012038 (2014).

[11] A. M. P. Mendez, C. C. Montanari, and J. E. Miraglia, *Ionization of Biological Molecules by Multicharged Ions Using the Stoichiometric Model*, J. Phys. B: At. Mol. Opt. Phys. **53**, 055201 (2020).

[12] S. Sato, Z. He, M. Kaneda, M. Imai, H. Tsuchida, and A. Itoh, *Electron Energy Spectra from Various Amino Acids Bombarded by 2.0MeV He^+ Ions*, Nuclear Instruments and Methods in Physics Research Section B: Beam Interactions with Materials and Atoms **256**, 506 (2007).

[13] B. J. Whitaker, *Imaging in Molecular Dynamics Edited by Benjamin J. Whitaker*, https://doi.org/10.1017/CBO9780511535437.

[14] C. Bordas, F. Paulig, H. Helm, and D. L. Huestis, *Photoelectron Imaging Spectrometry: Principle and Inversion Method*, Review of Scientific Instruments **67**, 2257 (1996).

[15] A. T. J. B. Eppink and D. H. Parker, *Velocity Map Imaging of Ions and Electrons Using Electrostatic Lenses: Application in Photoelectron and Photofragment Ion Imaging of Molecular Oxygen*, Review of Scientific Instruments **68**, 3477 (1997).

[16] D. Nandi, V. S. Prabhudesai, and E. Krishnakumar, *Velocity Map Imaging for Low-Energy Electron–Molecule Collisions*, Radiation Physics and Chemistry **75**, 2151 (2006).

[17] Special Topic: Developments and applications of velocity map imaging techniques, The Journal of Chemical Physics **147**, 1 (2017).

[18] N. F. Ramsey, *Thermal Beam Sources*, in *Experimental Methods in the Physical Sciences*, Vol. 29 (Elsevier, 1996), pp. 1–20.

[19] M. Galanti, R. Gott, and J. F. Renaud, *A High Resolution, High Sensitivity Channel Plate Image Intensifier for Use in Particle Spectrographs*, Review of Scientific Instruments **42**, 1818 (1971).

[20] M. Sataka, J. Urakawa, and N. Oda, *Measurements of Double Differential Cross Sections for Electrons Ejected by 5-20 KeV H^+, H_2^+ and He^+ impacts on Argon*, J. Phys. B: At. Mol. Phys. **12**, L729 (1979).
[21] K. Jorgensen, N. Andersen, and J. O. Olsen, *Autoionising Levels in Argon Excited by Low-Energy Heavy-Ion Impact*, J. Phys. B: At. Mol. Phys. **11**, 3951 (1978).
[22] L. Sarkadi, *Classical Trajectory Monte Carlo Model Calculations for Ionization of the Uracil Molecule by Impact of Heavy Ions*, J. Phys. B: At. Mol. Opt. Phys. **49**, 185203 (2016).